Electrophysiological Signature Reveals Laminar Structure of the Porcine Hippocampus

Alexandra V. Ulyanova[*1], Paul F. Koch[*1], Michael R. Grovola[1,2], Kevin D. Browne[1,2], Robin J. Russo[1], Christopher D. Adam[1], Douglas H. Smith[1], H. Isaac Chen[1,2], Victoria E. Johnson[1], D. Kacy Cullen[#1,2], and John A. Wolf[#^1,2]

[1] Department of Neurosurgery, University of Pennsylvania, Philadelphia, PA

[2] Corporal Michael J. Crescenz Veterans Affairs Medical Center, Philadelphia, PA

[^]corresponding author

[#]authors contributed equally to the support of this work

*authors contributed equally to this work

Running title: Laminar structure and electrophysiology of pig hippocampus

Corresponding Author:
John A. Wolf, Ph.D.
Dept. of Neurosurgery
Perelman School of Medicine
172A Stemmler Hall
3450 Hamilton Walk
Philadelphia, PA, 19104
+1-(215)-746-4680
wolfjo@upenn.edu

Grant sponsor: The Department of Veterans Affairs; Grant number: IK2-RX001479, I01-RX001097. Grant sponsor: The National Institutes of Health; Grant number: NINDS R01- NS-101108-01, T32-NS043126). Grant sponsor: CURE Foundation; Grant number: Taking Flight Award. Grant Sponsor: DoD ERP CDMRP; Grant Number: W81XWH-16-1-0675.

Key Words: hippocampal cytoarchitecture, *in vivo* electrophysiology, pig, silicon probes

Abstract

The hippocampus is involved in aspects of both working and episodic memory, and is a central region of interest in diseases affecting these processes. While the role of the hippocampus in memory is studied predominantly in rodents, rodent neurological disease models have not historically translated well to human treatment. Non-human primate disease models, while highly translational, present both economic and ethical challenges. Therefore, an alternative research model is required to study memory and cognition during development and to follow disease progression. Because pig models are widely used in other translational research, they may provide an excellent compromise between rodents and non-human primates due in part to the gyrencephalic neuroanatomy and significant white matter composition of the porcine brain. In addition, the porcine hippocampal anatomy and cytoarchitecture more closely resembles that of primates than rodents. To advance the study of the neurophysiology of the pig hippocampus and related structures, we utilized stereotaxis combined with single-unit electrophysiological mapping to precisely place laminar silicon depth probes into the dorsal hippocampus of miniature pigs without the need for image guidance. We then implemented an *in vivo,* electrophysiology-based methodology to identify hippocampal layers and to examine hippocampal neurophysiology using these depth probes. This methodology allowed for the simultaneous recording of laminar field potentials and single-cell activity in multiple layers in the dorsal hippocampus. The laminar structure of dorsal hippocampus and the precise location of the probes were confirmed by electrophysiology and histopathology, eliminating the need to recover electrode tracks in future animals. This methodology allows us to investigate hippocampal electrophysiology under anesthesia, with potential expansion into awake behaving neurophysiology. Accessible neurophysiology of the pig hippocampus may allow for the development of new translational models of neurological disorders, with the possibility of evaluating the neuronal and circuitry disruptions that underlie cognitive and memory dysfunction.

Introduction

The foundations of experimental neuroscience are largely rodent and non-human primate neuroanatomy, neurophysiology and neurochemistry. Advances in medicine and bioengineering have begun to complement the explosion in knowledge describing both normal neural function and the mechanisms of neurological disease, creating a need for robust, practical pre-clinical models of the human nervous system to test novel therapies. Given the regular failure to translate to the clinic many therapies that were successful in rodents, as well as the expense and ethical challenges of non-human primate experimentation, a need for practical alternatives has emerged (Goodman and Check, 2002).

Pigs models are already well-established in biomedical research in the areas of toxicology, drug discovery, exercise physiology, obesity, diabetes, cardiovascular disease, experimental surgery, and traumatic brain injury (Cullen et al., 2016; Johnson et al., 2015; Kimura et al., 1996; Larsen and Rolin, 2004; Lehmann, 1998; Richer et al., 1998). Due to their anatomical and physiological resemblance to humans, wide-spread commercial production and the lower procurement costs, pigs are preferably used as an animal model in the areas of cardiovascular, orthopedics and wound-healing research (Walters et al., 2017). Genetically stable stocks of miniature pigs are already available and currently used in a wide range of laboratory settings, including neuroscience research endeavors (Lind et al., 2007; Sorensen et al., 2011). Genetically altered pigs have been engineered for clinical models of human diseases such as cystic fibrosis and heart arrhythmias (Park et al., 2015; Rogers et al., 2008). Further, the combination of genetic engineering and physiological similarities suggests that pigs may be an ideal substrate for organ xenotransplants to humans (Hering et al., 2016).

Rodents and non-human primates have been the most prevalent animal models with which to study neurological deficits involving the hippocampus such as memory disruption following traumatic brain injury, neurodegeneration, and epilepsy (Buzsáki, 2015; Jang and Chung, 2016; Levin, 2003). Despite a vast body of experimental and descriptive literature, rodent models of neurological pathophysiology have not historically translated well to clinical treatments, particularly in some disease models. While use of non-human primates reduces the problems due to species differences, these models are limited by economic and ethical restraints (Goodman and Check, 2002). Recently, pigs have been proposed as another model for translational neuroscience research, given their size, the gyrencephalic aspects of the porcine brain with significant white matter composition, and hippocampal features such as its position in the brain, a laminated hilus and a dispersion of the pyramidal cells into stratum oriens similar to

those of non-human primates (Holm and West, 1994; Lind et al., 2007; Sorensen et al., 2011). Pig behavior is known to be extremely complex, as pigs are able to perform sophisticated memory and other cognitive tasks, exhibit complex social behaviors, and even show some limited abilities that are a prelude to self-awareness (Broom et al., 2009; Gieling et al., 2011a). Much of the basic neuroanatomical characterization of the porcine brain and the hippocampus in particular has been done using both histological and clinical imaging methods such as positron emission tomography and magnetic resonance imaging (MRI) (Lind et al., 2007; Rogers et al., 2008). The anatomy of the porcine brain has many features of the primate brain, including similarities in hippocampal structure (Holm and West, 1994). Although an extensive immunohistological characterization of cell types within the porcine hippocampus of the domestic pig (Danish Landrace) has been published previously, the dorsal hippocampus of Yucatan miniature pigs used for this study has not been characterized histologically or electrophysiologically (Holm and Geneser, 1991; Holm et al., 1992; Holm et al., 1993; Holm et al., 1990). Further, experimental and preclinical functional studies in both normal and pathophysiological states have been undertaken using functional MRI, electroencephalography and most recently both *in vivo* and *ex vivo* electrophysiology (Van Gompel et al., 2011; Wolf, 2017).

Pigs therefore have the potential to be an excellent preclinical model for the development of therapies for the hippocampal network and other regions, including electrical and chemical neuromodulation and the stereotactic delivery of viral gene products, or drugs. One key next step is the ability to conduct *in vivo* electrophysiological studies utilizing precisely placed high density depth electrodes capable of recording laminar activity, which requires precision large animal stereotaxis. Several image-guided stereotactic instruments have been previously developed for pigs (Ettrup et al., 2011; Marcilloux et al., 1989; Poceta et al., 1981; Szteyn et al., 1980), along with a number of stereotactic atlases of the pig brain (Felix, 1999; Saikali et al., 2010; Salinas-Zeballos, 1986; Szteyn et al., 1980; Watanabe et al., 2001). Approaches based on skull landmarks have been implemented in order to place probes in the dorsal and ventral hippocampus of miniature pigs (Saito et al., 1998). However, variations in skull structure (thickness and suture landmarks) between strains as well as age-dependent changes in these anatomical relationships create inconsistency in stereotactic procedures relying exclusively on bone landmarks. While these complications can be overcome by the placement of MRI-compatible localizers of cranial landmarks, or ventriculography, they increase the cost and time of *in vivo* procedures significantly and are not available at all institutions (Bjarkam et al., 2004; Marcilloux et al., 1989; Van Eerdenburg and Dierx, 2002).

We therefore implemented stereotaxis without the necessity of imaging to precisely place depth probes into the dorsal hippocampus of miniature pigs. More specifically, we developed a methodology that allows for the localization and study of porcine hippocampal electrophysiology under anesthesia to identify hippocampal layers and to record hippocampal activity. We described some of the basic characteristics of the electrophysiological laminar structure of the porcine hippocampus using high density silicon based laminar probes, including simultaneous recordings of single unit activity and local field potentials. We confirmed the laminar structure of the hippocampus and the precise location of the 32-channel silicon probe using both electrophysiology and histopathology, eliminating the need to recover electrode tracks in future animals, thus allowing valuable tissue to be used for other studies. We examined potential strain and age-related differences and confirmed histologically that the neuroanatomy of the miniature swine hippocampus has many features of the human hippocampus by staining sagittal and coronal sections as described previously (Johnson et al., 2013a). This methodology will ultimately allow for the potential expansion of hippocampal neurophysiology into awake behaving pigs under normal conditions, as well as in models of pathophysiological conditions such as traumatic brain injury and epilepsy.

Materials and Methods

Animals and Animal Care

In the current study, we used Yucatan miniature pigs, which are known for their docile temperament, ease of handling, and slow growth rate (NSRRC Cat# 0012, RRID:NSRRC_0012). Pigs were purchased from Sinclair and underwent the current studies at the approximate age of 5-6 months at a mean weight of 21±3 kg (n=5). We chose this age as the pigs are post-adolescence with almost fully developed brains, but young enough to be of a manageable weight for procedures and behavior (Duhaime et al., 2000; Flynn, 1984; Pampiglione, 1971). All pigs were pair housed when possible, but always in a shared room with other pigs. All experiments were conducted according to the ethical guidelines set by the Institutional Animal Care and Use Committee of the University of Pennsylvania, an AAALAC certified research facility.

Placement in Novel Stereotactic Frame

The stereotactic frame consisted of four major components: frame base, bite plate, anterior-posterior (AP) bars, and skull pins (Figure 2C, see below). The frame base (1) hold all parts of the stereotax and was made of heavy aluminum alloy with holes to attach the AP bars of the stereotactic frame. As the animal was guided into the stereotactic frame, its jaw was opened and its maxilla placed on top of the bite bar (2) with the endotracheal tube positioned below the bar. The point at which the bite bar meets the frame base was adjustable. Additionally, the bite bar could be maneuvered in the AP plane and rotated in the coronal plane, allowing the researcher to optimally position the head prior to pin insertion. The AP bars (3) were independent parallel rails fastened to the frame base and run parallel to the animal's head in the sagittal plane. These arms had standard 1 mm markings. Stereotactic manipulator arms (Kopf Instruments, Cat# 1760) could then be secured to the AP bars and moved along them in the AP plane using the Vernier scale to 0.1 mm precision. Before securing the animal with the skull pins, two points on each side of the animal along the zygoma, approximately 3 cm apart, were sterilely prepped with chlorhexidine solution and a small stab incision of 2-3 mm made at each point with a scalpel. Four stainless steel pins (4) affixed to the frame were inserted into the zygoma at each of these points providing rigid fixation of the head to the frame. In order to position the head precisely for stereotactic localization, each of these pins could be moved in three dimensions while the pig was secured in the stereotax.

An angle of 10-12° between the skin above the dorsal surface of the skull and the base of the stereotax was initially selected so that the cortical surface above the hippocampal region is level with the AP bars (Figure 2B, dashed line, see below). Following initial alignment and skull fixation of the animal in the stereotactic frame to achieve this angle, the animal's head was re-positioned again after skin incision based on fine measurements of the skull surface and bregma. An electrode holder with a marking pin was assembled and zeroed to bregma and the skull surface. In order to level the skull in the coronal plane, the dorsal-ventral (DV) coordinates were first measured in the medial-lateral (ML) plane. Head angle was finely adjusted if the difference in the DV coordinates on each side of the skull at ML=10 mm was more than 0.5 mm. Next, the DV coordinates were measured in the midline at bregma and AP=+30 mm. The angle between the skull surface and the base of stereotax was finely adjusted by repositioning the pins until the difference in the DV measurements at these two points was no more than 2.9±0.1 mm, which corresponds to an angle of 7°. We found this angle to be ideal for reproducibly locating and mapping the dorsal hippocampus.

Surgical Procedure

Yucatan miniature pigs were fasted for 16 hours then induced with 20 mg/kg of ketamine and 0.5 mg/kg of midazolam. Animals were intubated with an endotracheal tube and anesthesia was maintained with 2-2.5% isoflurane per 2 liters O_2. Each animal was placed on a ventilator and supplied oxygen at a tidal volume of 10 mL/kg. A catheter was placed in an auricular vein to deliver 0.9% normal saline at 200 mL per hour. Additionally, heart rate, respiratory rate, arterial oxygen saturation, end tidal CO_2 and rectal temperature were continuously monitored, while pain response to pinch was periodically assessed. All of these measures were used to titrate ventilation settings and isoflurane percentage to maintain an adequate level of anesthesia. A forced air warming system was used to maintain normothermia throughout the procedure.

Three pigs in this study underwent electrophysiological recordings and analysis. These pigs were placed in a stereotactic frame (described below), with the surgical field prepped and draped. A linear incision was made along the midline. A 13 mm diameter burr hole was made centered at 7 mm lateral to the midline and 4.5 mm posterior to bregma. The bony opening was subsequently expanded using Kerrison punches. The dura was opened in a cruciate manner using a #11 blade. We then "mapped" the dorsal hippocampus with several electrode insertions in the sagittal plane, utilizing observed spiking activity to generate a two-dimensional map (Figure 2D, see below). For this mapping, we used a high impedance tungsten monopolar electrode (∅ = 125 μm, length = 60 mm, impedance = 0.5 MΩ, FHC, Cat# UEWSEGSEBNNM).

A skull screw was placed over the contralateral cortex as a reference signal. For one of the pigs, we then chose coordinates within this map for insertion of a linear 32-channel silicon electrode with 200 μm spacing (NeuroNexus, Cat# V1x32-Edge-10mm-200-312-Ref) such that the linear spread of electrode contacts would span the laminar structure of the dorsal hippocampus at its maximal thickness in the dorsal-ventral plane, perpendicular to the individual hippocampal layers. The silicon probe is designed with one low-impedance channel placed 2 mm above the next most-proximal channel, which we used as a reference signal. For dorsal hippocampal targeting, this usually results in the reference channel being positioned within the temporal horn of the lateral ventricle sitting just above the hippocampus. This provided 31 channels for intra-hippocampal recordings. We implanted another animal with a similar 32-channel silicon electrode, but the spatial arrangement of the 31 intra-hippocampal channels were of a custom design (NeuroNexus, Cat# V1x32-15mm-tet-lin-177, data not shown). At the end of the procedure the anesthetic level was deepened and pigs were sacrificed for histological analysis.

Neural Data Collection and Analysis

All electrophysiological recordings were made under isoflurane anesthesia. Neural signals were amplified and acquired continuously at 32 kHz on a 64-channel Digital Lynx 4SX acquisition system with Cheetah recording and acquisition software (Neuralynx, Inc.).

Spike Detection and Analysis: Signals acquired from the tungsten monopolar electrode during the mapping procedure were bandpass filtered (600 Hz to 6 kHz) and thresholded for spike detection in real time. Thresholds were chosen based on observed signal to noise ratios during the session. Recorded spike trains and waveforms then underwent off-line automated spike sorting using KlustaKwik software (http://klusta-team.github.io/klustakwik/, RRID:SCR_014480) and further manual refinements using SpikeSort3D (Neuralynx, Inc.). Neural signals acquired from the 32-channel silicon probe were bandpass filtered (0.1 Hz to 9 kHz) in real time prior to sampling. Off-line spike detection and sorting was performed on the wideband signals using the Klusta package (http://klusta-team.github.io/klustakwik/, RRID:SCR_014480), which was developed for higher density electrodes, and manually refined with KlustaViewa software (https://github.com/klusta-team/klustaviewa). The Klusta routines are designed to take advantage of the spatial arrangement of and spike timing from all probe channels simultaneously in constructing putative clusters (Rossant et al., 2016). Resulting single-unit clusters were then imported into Matlab software, version R2017a for visualization and further analysis using custom and built-in routines (https://www.mathworks.com/products/matlab.html, RRID:SCR_001622). In order to minimize

waveform shape distortion for visualization, the wideband signal was high pass filtered using a wavelet multi-level decomposition and reconstruction filter (level 6, Daubechies 4 wavelet) (Wiltschko et al., 2008). Waveforms were then extracted from this filtered signal and averaged for display.

Analysis of Local Field Potentials (LFP): Acquired wideband LFP recorded with the 32-channel silicon probe were downsampled to 2 kHz for further analysis. Signals were imported into Matlab software, version R2017a (https://www.mathworks.com/products/matlab.html, RRID:SCR_001622) and processed using a combination of custom and modified routines from the freely available Matlab packages FMAToolbox (http://fmatoolbox.sourceforge.net) and Chronux (http://chronux.org**,** RRID:SCR_005547**)** (Hazan et al., 2006; Mitra, 2007). For spectral power analysis, 3 minute recordings from all 31 hippocampal channels were broken into 1 second segments. Each segment underwent multi-taper spectral analysis in the frequency range of 100 Hz to 200 Hz at each channel (Chernyy et al., 2008). The power for each 1 second segment at each channel was then integrated over the entire frequency range. The values for each channel were then averaged across all 1 second segments resulting in the average integrated spectral power as a function of probe depth.

For detection of "cortical bursts", the wideband LFP in the most distal channel was squared and then z-score normalized (Amzica, 2015). Samples with amplitudes greater than 5 standard deviations above the mean were selected. As multiple samples within the same "burst" event could qualify, a minimum separation of 50 msec was imposed for each event. LFP data segment of 200 msec from all 31 channels surrounding each qualifying event was then extracted and averaged. Current source density (CSD) was then calculated for this averaged "burst" event as the second spatial derivative of the LFP across all 31 hippocampal channels and visualized by convention as a heat map of current sinks (blue) and sources (orange) (Mitzdorf, 1985).

Tissue Handling and Histological Examinations

Histological analyses were performed on brain tissue from Yucatan miniature pigs (n=5 total) in order to locate tracks generated by electrode insertion (n=3), as well as to histologically characterize the porcine hippocampus (n=2). While under isoflurane anesthesia, all animals underwent transcardial perfusion with 0.9% heparinized saline followed by 10% neutral buffered formalin (NBF). After post-fixation for 7 days in 10% NBF at 4°C, each brain was dissected into 5 mm blocks in the coronal (n=3) or sagittal (n=2) plane and processed to paraffin using standard techniques. 8 µm sections were obtained at the level of the hippocampus in either the

coronal or sagittal plane. Standard hematoxylin & eosin (H&E) staining was performed on all animals to visualize electrode tracks.

Luxol Fast Blue / Cresyl Violet (LFB/CV) Staining: Tissue sections were dewaxed in xylenes and rehydrated to water via graded ethanols before being immersed in 1% LFB solution (Sigma, S3382) at 60°C for 4 hours. Excess stain was then removed by immersion of sections in 95% ethanol. Differentiation was performed via immersion in 0.035% lithium carbonate for 10 seconds followed by multiple immersions in 70% ethanol until the gray and white matter could be clearly distinguished. Slides were rinsed and counterstained via immersion in preheated 0.1% CV solution (Sigma, C5042) for 5 minutes at 60°C. After further rinsing, slides were differentiated in 95% ethanol with 0.001% acetic acid, followed by dehydration, clearing in xylenes and cover slipping using cytoseal-60.

Immunohistochemistry (IHC): Single IHC labeling was performed according to previously published protocols (Johnson et al., 2013a). Briefly, tissue sections were dewaxed in xylenes, rehydrated to water via graded ethanols and immersed in 3% aqueous hydrogen peroxide for 15 minutes to quench endogenous peroxidase activity. Antigen retrieval was achieved via microwave pressure cooker at high power for 8 minutes, submerged in Tris EDTA buffer (pH 8.0). Sections were then incubated overnight at 4°C using antibodies specific for MAP2 (Abcam, Cat# ab5392 Lot# RRID:AB_2138153, 1:1000), parvalbumin (Millipore Cat# MAB1572 Lot# RRID:AB_2174013, 1:1000), and the N-terminal amino acids 66–81 of the amyloid precursor protein (APP) (Millipore, Cat# MAB348 Lot# RRID:AB_94882, 1:80K). Slides were then rinsed and incubated in the relevant species-specific biotinylated universal secondary antibody for 30 minutes at room temperature. Next, application of an avidin biotin complex (Vector Laboratories, Cat# PK-6200 Lot# RRID:AB_2336826) was performed for 30 minutes, also at room temperature. Lastly, the 3, 3'-diaminobenzidine (DAB) peroxidase substrate kit (Vector Laboratories, Cat# SK-4100 Lot# RRID:AB_233638) was applied according to manufacturer's instructions. All sections were counterstained with hematoxylin, dehydrated in graded ethanols, cleared in xylenes, and cover slipped using cytoseal-60.

Slide Imaging

Whole brain coronal tissue sections were digitally scanned at 20X magnification using the Aperio CS2 Digital Pathology Scanner (Leica Biosystems). Additional images were captured on a Nikon Eclipse 80i upright microscope and a DSRi1 camera (Nikon, Inc.), with associated NIS-Elements software, version V4.5 (https://www.nikoninstruments.com/Products/Software, RRID:SCR_014329).

Results

Neuroanatomy of Porcine Hippocampus

In order to plan our initial stereotactic approach to the dorsal hippocampus in the Yucatan minipig, we first undertook a gross anatomical and histological study of the structure. Three Yucatan miniature pigs were sacrificed and the brains extracted (see Methods). Figure 1A shows the sulci, multiple gyri and white/gray matter composition of the porcine brain in coronal section stained with CV, highlighting subcortical structures such as the hippocampus and thalamus that are stereotactically accessible from the brain surface. Analogous to rodent and human hippocampus, porcine hippocampus is oriented so that both coronal and sagittal planes produce arrow-like structures from anatomical layers in a similar orientation, as shown with LFB staining in Figure 1B. The granule cells of the dentate gyrus form the point of the arrow, the notably large hilar region in pigs forms the body of the point and the pyramidal cells of the cornu ammonis (CA) regions form the curved shaft in both planes. The classic hippocampal layers (alveus, striatum oriens, stratum pyramidale, striatum radiatum, striatum lacunosum-moleculare, striatum moleculare, and stratum granulosum), as well as the hippocampal fissure, which divides the dentate from the CA regions, are clearly visible under higher magnification (Figure 1C-E). Staining with LFB/CV highlights myelinated fibers and neuronal cell bodies in the pyramidal and granular cell layers, revealing the expected ordered orientation of these fibers in relation to the cell bodies, a feature that plays critically in the laminar interpretation of hippocampal electrophysiology (Figures 1C, F). However, in contrast to rodent anatomy, the pyramidal CA1 cell layer appears less densely packed in pigs and more analogous to primate hippocampus, due to a progressive dispersion of these cells into stratum oriens in the direction of the subiculum as previously reported (Holm and West, 1994). This dispersion has the effect of partially blurring the distinction between stratum pyramidale and the most dorsal aspects of stratum radiatum, as synaptic inputs into the dendritic tree of the more dorsally-located cells will co-localize with the more ventrally-located cell bodies. This phenomenon can be readily seen with MAP2 labelling, showing pyramidal cells above the main CA1 layer sending dendrites through stratum pyramidale into the distal layers (Figure 1D, G). These dendritic arbors are very dense and intermingled. Finally, as previously reported in another strain of pig, a sub-population of interneurons located in the pyramidal and dentate granular cell layers can be identified with Parvalbumin (PV^+) staining (Figure 1E, H) (Holm et al., 1990). These PV^+ positive interneurons primarily located above, inside, and below the pyramidal CA1 layer also have deep projections into the radiatum.

Novel Porcine Stereotaxis

Although stereotactic approaches based on skull landmarks, or on individual subject imaging, have been designed for *in vivo* electrophysiological studies in pigs, they are either inconsistent, expensive to utilize, or difficult to implement (Felix, 1999; Marcilloux et al., 1989; Saito et al., 1998). Our goal was to design a relatively inexpensive stereotactic system using electrophysiological localization without the need for individual subject imaging in order to accomplish *in vivo* electrophysiological recordings in pigs. Based on previous stereotactic work in our laboratory we chose to select bregma as the starting landmark for our stereotaxis. Bregma is defined as an anatomical point on the skull, at which the coronal sutures intersect with the sagittal suture at the midline. Although the relationship between bregma and the underlying brain can vary by several millimeters rostral to caudal (i.e. along the sagittal plane), the principle advantage is that bregma can be easily identified during surgery. We therefore defined the two-dimensional medial-lateral (ML) and anterior-posterior (AP) zero point to be bregma. Based on our previous experience we identified the approximate level of bregma in the coronal and sagittal planes on a freely available three-dimensional MRI atlas of the pig brain (Saikali et al., 2010). Figure 2A shows the orientation of the cortex and deeper structures, such as the dorsal and ventral hippocampus and the thalamus, at this level on the MRI atlas. Based on this MRI atlas, we then chose 7 mm lateral to the midline as the sagittal plane that maximized CA1 thickness and aligned the dorsal hippocampal laminar structure perpendicularly with the cortical surface. Note that the Yorkshire (another domestic pig strain) MRI atlas coronal section is structurally similar to a representative coronal section of the Yucatan brain used in this study, with slight shape variations due to strain differences (Figures 1A and 2A).

Because the position of bregma in the AP plane with respect to the brain varies between animals, we selected an approximate range of AP coordinates that spans the AP extent of the dorsal hippocampus on the MRI atlas, approximately 12 mm in total. A sagittal section through ML 7 taken from the MRI atlas shows the position and approximate size of the dorsal hippocampus (Figure 2B, horizontal line). The image is rotated so that cortical surface above the hippocampus is horizontal. Again, the sagittal section obtained from the MRI atlas is similar to the sagittal histological section of porcine brain used in our study (Figure 1B, bottom). This section of brain defined by the AP extent of the dorsal hippocampus at ML 7 then became the section of interest for electrophysiological mapping during surgery (see below).

We constructed a novel stereotactic frame based on percutaneously placed skull pin fixation, a commonly employed technique in human neurosurgery (Figure 2C). We used an

iterative process of progressively finer adjustments both before and after skull pin fixation to place the pig's head precisely within the frame at a consistent angle such that the dorsal surface of the brain above the hippocampus was parallel to the base of the stereotactic frame (see Methods). The pig was first positioned approximately within the frame using a bite bar. Four skull pins were then inserted through the skin into the bone of bilateral zygomas, fixing the head. The head was then further adjusted to the desired angle using the skull pins, which can be moved in three dimensions. A final fine adjustment to the skull angle was made via direct measurements on the surface of the skull using a stereotactic arm and measurements on the frame once the skull had been exposed.

Electrophysiological Mapping

Since the initial, atlas-based coordinates selected for electrode placement can be inaccurate due to skull and individual animal variation as well as minor brain swelling during surgery, the precise location of the hippocampus needs to be determined within the stereotactic space. We utilized electrophysiological mapping based on microelectrode mapping techniques used in human deep brain stimulation (DBS) surgery (Gross et al., 2006). An electrophysiological map of the cortex, dorsal hippocampus and top of the thalamus was created by driving a small diameter (125 μm) high impedance electrode into the brain and recording the coordinates at which neuronal spiking activity was detected. As discussed above, we expected variability in location of the hippocampus primarily in the AP plane. Therefore, mapping in the first animal was executed in the sagittal plane at ML 7 by advancing the electrode in equal steps in the AP plane in 2 mm intervals. In this manner, we drove the electrode from the brain surface (DV=0) to a final depth of 30 mm (DV=30). At each AP level, we notated where neuronal spiking activity was detected, thereby creating a two-dimensional map of the dorsal hippocampus and surrounding structures in the sagittal plane (Figure 2D, circles). The map of spiking activity generated an outline of the ventricle, dorsal hippocampus, thalamus and overlying cortex (Figure 2D, lines), which can be compared to a representative sagittal section stained with LFB (Figure 2E). To confirm this result in our first pig, blue dye was stereotactically injected at the corresponding mapped AP coordinates to a depth of 30 mm. A representative sagittal section from this brain, stained with H&E, demonstrates tracks from the injecting syringe (Figure 2F, dashed lines), confirming correct localization of the mapping procedure within the hippocampus. The most superficial point within the hippocampus where neuronal spiking activity was detected, corresponding either to neurons within stratum oriens, or

to the pyramidal CA1 layer was located 18.5±1.8 mm (mean ± stdev, n = 4) below the brain surface.

Hippocampal Laminar Structure and Electrode Localization

Single Unit Spiking Activity: Once this technique became routine, we were able to use fewer tracks on subsequent animals (as few as three) to localize the hippocampus in sagittal profile. Figure 3 shows a small portion of the electrophysiological map within the hippocampus generated on a subsequent pig. In this experiment, after generating a larger map that localized the position of the hippocampus, we advanced the high impedance electrode along the depicted DV track in 100-200 μm intervals, recording for 3 minutes at each level. We then isolated putative single units off-line. Circles in Figure 3 indicate DV coordinates where single unit activity was isolated. A larger 32-channel silicon probe was then inserted to a DV position of 25 along this same track (Figure 3). The stereotactic coordinates of this probe as well as of the generated map, along with the histological artifact generated by the silicon probe (Figure 3, black arrow), allowed us to approximately align the map of recorded single unit activity with a representative coronal section stained histologically with LFB/CV (coronal plane). This single electrode data revealed a cluster of single unit activity aligned with the diffuse pyramidal cell layer depicted in the histology and a second cluster of single unit activity aligned to the edge of the dentate gyrus at the granular cell layer and hilus. While various cell types in the hippocampus of the domestic pig have been identified with immunohistological markers previously, their electrophysiological characteristics are unknown (Holm et al., 1992; Holm et al., 1993; Holm et al., 1990). Here we report representative average waveforms and firing rates of putative single neuron action potentials within the various porcine hippocampal layers (Figure 3). These findings together illustrate how our mapping procedure defines the individualized hippocampal anatomy along with the electrophysiology and allows for precision placement of subsequent electrodes, including high-density silicon probes.

Simultaneous Laminar Field Potentials and Single Unit Activity via High Density Silicon Probe: Unlike rodent studies in which electrode tracks are routinely recovered for each experiment, the brain tissue from large animals is usually utilized for multiple neuropathological studies, particularly in central nervous system (CNS) disease models. In addition to being time and resource intensive to recover electrode tracks due to the large size of the pig brain, this tissue is then no longer available for neuropathological studies. To eliminate the need to recover electrode tracks in future animals, we here describe an electrophysiological analysis to localize

multi-channel electrodes to the pyramidal CA1 cell layer and other hippocampal laminar structures during insertion.

A linear 32-channel (31 recording sites, 200 μm spacing) silicon electrode was inserted into the dorsal hippocampus based on an initial mapping (Figure 4A). Once in position, we recorded from the electrode for 3 minutes. Several analyses of the local field potentials (LFP) help to confirm precise localization of the electrode within the hippocampus. First, inspection of a representative 6 seconds of wideband neural signals across the length of the probe reveals prominent multi-unit spiking activity in a band near the dorsal end of the electrode and a less-prominent band of spiking activity more ventrally (Figure 4B). This activity is also reflected in the isolated single unit activity (Figure 4E). Representative averaged waveforms and firing rates are depicted in Figure 4E. Although the single unit activity similarly splits into a larger, dorsally located band of activity and a smaller ventral band, it appears to be more diffuse when compared to the multi-unit activity seen within the wideband LFP.

Second, it has been reported that the power of higher frequency oscillatory activity in the hippocampal LFP within the 100 Hz – 200 Hz range is generated not only by coordinated synaptic input (primarily from interneurons), but by the action potentials of coordinated local pyramidal cell firing. Importantly, much of the power may come from action potentials of cells further than 100 μm away, making this signal detectable even when there are no neurons close enough to the recording electrode to result in isolatable single unit activity (Schomburg et al., 2012). Figure 4C shows integrated spectral power (100 Hz – 200 Hz) across channels, demonstrating a large peak at the level of the prominent multi-unit spiking activity, suggesting localization to the CA1 pyramidal layer.

Third, we took advantage of the periodic bursts (~1 Hz) of coordinated synaptic input across the entirety of the electrode (Figure 4B, blue asterisks). These bursts likely represent cortical bursts of synchronized activity known to occur periodically under anesthesia, and which are detectable within the hippocampal LFP (Amzica, 2015; Steriade, 1997). We reasoned that such large synchronized inputs might reveal a pattern of inward current flow consistent with the laminar structure of the hippocampus, aiding in localization. To this end we averaged a 200 msec LFP segment surrounding each detected burst. We then performed current source density (CSD) analysis on the resulting averaged LFP. The inward current sinks (blue) of the dendrites and the outward currents sources (orange, thought to arise from cell bodies) were aligned across the 31 channels of the electrode in Figure 4C (Mitzdorf, 1985; Nicholson and Freeman, 1975). Using the spatial distribution of sinks and sources, the bimodal distribution of multi- and

single unit activity, and the spectral power analysis discussed above, we were able to approximately align the electrode position with a representative histological section (coronal), confirmed by the histological artifact made by the electrode tip (not shown). Figure 4 depicts this alignment. Prominent, expected current sinks are seen in both the proximal dendritic tree of the CA1 pyramidal cells (stratum radiatum) and in the distal dendritic tree (stratum lacunosum-moleculare). There is also a mix of sinks and sources in the hilus, consistent with mossy fiber input from the dentate to the mossy cells and other hilar neurons (Bragin et al., 1995). There are expected associated sources within the pyramidal layer and in the region of the granular cell layer, which co-localize with the multi- and single unit activity (Figures 4B, E) as well as the peak high frequency spectral power (Figure 4C). These findings suggest that the probe spans the dorsal hippocampus from stratum oriens into the dentate and the hilus, confirming accuracy of intended placement (Figure 4C). Localized damage from the insertion of the electrode through the pyramidal CA1 cell layer was confirmed post mortem with LFB/CV staining (Figure 4A). Additionally, these electrode tracks were confirmed with APP labeling, which accumulates in injured axons (Gentleman et al., 1993; Johnson et al., 2013b; Sherriff FE, 1994) and may be useful for electrode track detection in acute experiments in other species (data not shown).

Discussion

In the past decade pigs have emerged as an attractive model for neuroscience research (Gieling et al., 2011b; Lind et al., 2007). Many studies have been conducted to investigate cognitive performance in pigs (Gieling et al., 2011a; Grimberg-Henrici et al., 2016; Sullivan et al., 2013b). Behavioral paradigms such as neurobehavioral assessment in piglets and novelty tests in young pigs have recently been developed (Broom et al., 2009; Fleming and Dilger, 2017; Sullivan et al., 2013a). Although rodents have been the prevalent animal to study neurological and behavioral deficits, these models have not translated well in most clinical applications, particularly with ischemic and traumatic brain injury (Aertker et al., 2016). While non-human primates and dogs have gyrencephalic brains, research conducted using these species generates strong ethical concerns and substantial public opposition (Goodman and Check, 2002). The pig has been proposed as a better alternative to some animal CNS disease models currently performed with other larger animal species, particularly non-human primates or dogs (Rollin, 2006).

Awake electrophysiological recordings in pigs have been reported in the past, and the promise of pigs for intracranial monitoring studies and *ex vivo* electrophysiology has increased recently (Conn, 1991; Van Gompel et al., 2011; Wolf, 2017). While several stereotaxic instruments have been developed for pigs, variations of skull landmarks due to age-depended changes can create inconsistency in stereotaxic procedures (Ettrup et al., 2011; Marcilloux et al., 1989; Poceta et al., 1981; Saito et al., 1998; Szteyn et al., 1980). These complications can be overcome by the placement of MRI-compatible localizers of cranial landmarks, or ventriculography, but these solutions significantly increase costs and complexity (Bjarkam et al., 2004; Marcilloux et al., 1989; Van Eerdenburg and Dierx, 2002). Therefore, the development of a cheaper, more reliable stereotactic solution without the necessity of imaging may facilitate more electrophysiological studies of the porcine brain structures including hippocampus.

Although an extensive immunohistological characterization of cell types in porcine hippocampus has been published previously, we histologically characterized the dorsal hippocampus of Yucatan miniature pigs to compare to these previous findings (Holm and Geneser, 1991; Holm et al., 1992; Holm et al., 1993; Holm et al., 1990). We have confirmed that the hippocampus of Yucatan miniature pigs has similar laminar structure, with a standard orientation of hippocampal layers. The dispersed pyramidal cells and the relationship between pyramidal CA1 cell bodies and their dendritic arbors, as well as PV^+ interneurons in oriens and the hilus are particularly interesting in relationship to the laminar electrophysiological analysis, in

addition to positioning the cytoarchitecture of the hippocampus between the rodent and primate (Holm et al., 1992).

We have developed an inexpensive, non-imaging based swine stereotaxis for *in vivo* electrophysiology, which is based on skull position, angle and landmarks and confirmed with electrophysiological mapping. Although stereotactic approaches based on image-based stereotaxis and skull landmarks and have been previously described in pigs, they are expensive and laborious to use or may be inconsistent without mapping due to skull thickness changes over the age of the animal (Marcilloux et al., 1989; Saito et al., 1998). While stereotactic coordinates for both dorsal and ventral hippocampus were successfully confirmed by dye injections, the hippocampus location needs to be confirmed independently when precise localization of layers is required for recordings or implantation (Saito et al., 1998). In order to accomplish this, we have implemented electrophysiological mapping based on DBS widely used for neurosurgical procedures (Gross et al., 2006). Using on DBS style mapping, we have re-created a digitized map of cortex and hippocampus by recording electrical activity of individual cells at various depths, and we have confirmed that electrophysiological activity of the hippocampus matches the anatomy using stereotaxic dye injections.

To simultaneously record from all layers of hippocampal structure, we have designed a laminar silicon multi-electrode probe to simultaneously record oscillatory field potentials and individual unit activity throughout the circuitry of the hippocampus. This “edge” probe has 32 equally spaced channels, with 200 μm between individual channels for a total coverage of 6 mm total in length, which is able to cover the laminar architecture of the dorsal hippocampus in the miniature pig. The electrode sites have a linear arrangement and have been strategically positioned at the edge of the probe to interface with healthy tissue upon probe insertion. As recovering electrode tracks is impractical in large animal neuropathological studies, we have validated an electrophysiological analysis to localize electrodes to the pyramidal CA1 cell layer, which reduces the need to recover electrode tracks prior to neuropathological assessment in future animals. We have simultaneously recorded electrophysiological activity of many individual cells, which are appropriately distributed in a laminar fashion as expected from hippocampal structure and from the laminar field structure. In addition, the silicon probe localization was confirmed with CSD analysis that identified the expected laminar field structure of corresponding hippocampal layers based on cortical bursts coming into hippocampus under anesthesia (Amzica, 2015; Bragin et al., 1995; Mitzdorf, 1985; Nicholson and Freeman, 1975). This allows

for silicon probe localization based on functional mapping and field potential analysis, preserving valuable tissue for neuropathological studies.

Electrophysiological changes have largely been studied in rodent models of TBI, including disruptions in long-term potentiation, synaptic plasticity and broadband power (Miyazaki et al., 1992; Paterno et al., 2015; Schmitt and Dichter, 2015; Villasana et al., 2015; Zhang et al., 2011). Our laboratory's efforts to understand and correct network disruptions after TBI illustrate how the pig can also be used as a translational model of neurological disorders, taking advantage of the methods described here. Specifically, we have observed hippocampal axonal and synaptic dysfunction as well as regional hyperexcitability in an *ex vivo* slice preparation following an established porcine model of TBI where diffuse axonal injury is the primary neuropathological finding (Cullen et al., 2016; Johnson et al., 2016; Meaney et al., 1995; Wolf, 2017). Importantly, the electrophysiological methods described here will permit the confirmation of these results in anesthetized and awake behaving swine using an *in vivo* electrophysiological procedure which utilizes laminar multi-electrode silicon probes that are stereotactically placed into the pig hippocampus. This methodology will further support investigations into hippocampal-centric translational models such as those being developed for the study of post-traumatic epilepsy, as well as laying the groundwork for closed loop neuromodulation-based therapies in these models.

To summarize, we have developed a methodology that allows for the study of porcine laminar hippocampal electrophysiology under anesthesia without the need for imaging based stereotaxis. We have histologically confirmed that the neuroanatomy of Yucatan porcine brain closely resembles previously reported hippocampal structure, with features of both rodent and primate hippocampus. In particular, we implemented MRI-free stereotaxis to precisely place depth probes into the dorsal hippocampus of miniature pigs, and developed electrophysiology-based methodology to identify hippocampal layers and to record hippocampal activity using laminar probes. This allows for simultaneous recordings of oscillatory field potentials and single-cell activity in the dorsal hippocampus. Laminar structure of hippocampus and the precise location of 32-channel silicon probes were confirmed by electrophysiology and histopathology, eliminating the need to recover electrode tracks in each animal. Therefore, this study is the first detailed electrophysiological characterization of the porcine hippocampus and its laminar structure, as well as the demonstration of methodology for laminar recordings in the acute setting using MRI-free stereotaxis and silicon laminar probes. We hope that this characterization of the miniature swine hippocampus and low-cost methodology for stereotactic localization of

the dorsal hippocampus will allow for greater use of these gyrencephalic mammals in translational models that affect hippocampal circuitry, neuronal activity, and plasticity, and that this technique will be adapted for other subcortical regions. This methodology allows for potential expansion into awake neurophysiology under normal conditions, as well as pathophysiological conditions such as TBI and associated epilepsies. The combination of complex behaviors generated by these animals and the detailed neurophysiology of the hippocampus may present an ideal “middle ground” for translational hippocampal-centric disease models prior to clinical trials.

References

Aertker BM, Bedi S, Cox CS, Jr. 2016. Strategies for CNS repair following TBI. Exp Neurol 275 Pt 3:411-426.

Amzica F. 2015. What does burst suppression really mean? Epilepsy & Behavior 49:234-237.

Bjarkam CR, Cancian G, Larsen M, Rosendahl F, Ettrup KS, Zeidler D, Blankholm AD, Østergaard L, Sunde N, Sørensen JC. 2004. A MRI-compatible stereotaxic localizer box enables high-precision stereotaxic procedures in pigs. Journal of Neuroscience Methods 139(2):293-298.

Bragin A, Jando G, Nadasdy Z, van Landeghem M, Buzsaki G. 1995. Dentate EEG spikes and associated interneuronal population bursts in the hippocampal hilar region of the rat. Journal of Neurophysiology 73(4):1691.

Broom DM, Sena H, Moynihan KL. 2009. Pigs learn what a mirror image represents and use it to obtain information. Animal Behaviour 78(5):1037-1041.

Buzsáki G. 2015. Hippocampal sharp wave-ripple: A cognitive biomarker for episodic memory and planning. Hippocampus 25(10):1073-1188.

Chernyy N, Schiff SJ, Gluckman BJ. 2008. Multi-taper transfer function estimation for stimulation artifact removal from neural recordings. Conference proceedings : ... Annual International Conference of the IEEE Engineering in Medicine and Biology Society. IEEE Engineering in Medicine and Biology Society. Conference 2008:2772-2776.

Conn P. 1991. Elsevier Science.

Cullen DK, Harris JP, Browne KD, Wolf JA, Duda JE, Meaney DF, Margulies SS, Smith DH. 2016. A Porcine Model of Traumatic Brain Injury via Head Rotational Acceleration. In: Kobeissy FH, Dixon CE, Hayes RL, Mondello S, editors. Injury Models of the Central Nervous System: Methods and Protocols. New York, NY: Springer New York. p 289-324.

Duhaime A-C, Margulies SS, Durham SR, O'Rourke MM, Golden JA, Marwaha S, Raghupathi R. 2000. Maturation-dependent response of the piglet brain to scaled cortical impact. Journal of Neurosurgery 93(3):455-462.

Ettrup KS, Tornøe J, Sørensen JC, Bjarkam CR. 2011. A surgical device for minimally invasive implantation of experimental deep brain stimulation leads in large research animals. Journal of Neuroscience Methods 200(1):41-46.

Felix BL, M.E.; Albe-Fessard, D.; Marcilloux, J.C.; and Laplace, J.P. 1999. Stereotaxic atlas of the pig brain. Brain Research Bulletin 49(1-2):1-137.

Fleming SA, Dilger RN. 2017. Young pigs exhibit differential exploratory behavior during novelty preference tasks in response to age, sex, and delay. Behavioural Brain Research 321:50-60.

Flynn T. 1984. Developmental changes of myelin-related lipids in brain of miniature swine. Neurochem Res 9(7):935-45.

Gentleman SM, Nash MJ, Sweeting CJ, Graham DI, Roberts GW. 1993. β-Amyloid precursor protein (βAPP) as a marker for axonal injury after head injury. Neuroscience Letters 160(2):139-144.

Gieling ET, Nordquist RE, van der Staay FJ. 2011a. Assessing learning and memory in pigs. Animal Cognition 14(2):151-173.

Gieling ET, Schuurman T, Nordquist RE, van der Staay FJ. 2011b. The Pig as a Model Animal for Studying Cognition and Neurobehavioral Disorders. In: Hagan JJ, editor. Molecular and Functional Models in Neuropsychiatry. Berlin, Heidelberg: Springer Berlin Heidelberg. p 359-383.

Goodman S, Check E. 2002. The great primate debate. Nature 417(6890):684-7.

Grimberg-Henrici CGE, Vermaak P, Elizabeth Bolhuis J, Nordquist RE, van der Staay FJ. 2016. Effects of environmental enrichment on cognitive performance of pigs in a spatial holeboard discrimination task. Animal Cognition 19:271-283.
Gross RE, Krack P, Rodriguez-Oroz MC, Rezai AR, Benabid A-L. 2006. Electrophysiological mapping for the implantation of deep brain stimulators for Parkinson's disease and tremor. Movement Disorders 21(S14):S259-S283.
Hazan L, Zugaro M, Buzsáki G. 2006. Klusters, NeuroScope, NDManager: A free software suite for neurophysiological data processing and visualization. Journal of Neuroscience Methods 155(2):207-216.
Hering BJ, Cozzi E, Spizzo T, Cowan PJ, Rayat GR, Cooper DKC, Denner J. 2016. First update of the International Xenotransplantation Association consensus statement on conditions for undertaking clinical trials of porcine islet products in type 1 diabetes—Executive summary. Xenotransplantation 23(1):3-13.
Holm IE, Geneser FA. 1991. Histochemical demonstration of zinc in the hippocampal region of the domestic pig: II. Subiculum and hippocampus. The Journal of Comparative Neurology 305(1):71-82.
Holm IE, Geneser FA, Zimmer J. 1992. Somatostatin- and neuropeptide Y-like immunoreactivity in the dentate area, hippocampus, and subiculum of the domestic pig. The Journal of Comparative Neurology 322(3):390-408.
Holm IE, Geneser FA, Zimmer J. 1993. Cholecystokinin-, enkephalin-, and substance P-like immunoreactivity in the dentate area, hippocampus, and subiculum of the domestic pig. The Journal of Comparative Neurology 331(3):310-325.
Holm IE, Geneser FA, Zimmer J, Baimbridge KG. 1990. Chapter 7 Chapter Immunocytochemical demonstration of the calcium-binding proteins calbindin-D 28k and parvalbumin in the subiculum, hippocampus and dentate area of the domestic pig. Progress in Brain Research 83:85-97.
Holm IE, West MJ. 1994. Hippocampus of the domestic pig: A stereological study of subdivisional volumes and neuron numbers. Hippocampus 4(1):115-125.
Jang S-S, Chung HJ. 2016. Emerging Link between Alzheimer's Disease and Homeostatic Synaptic Plasticity. Neural Plasticity 2016:7969272.
Johnson VE, Meaney DF, Cullen DK, Smith DH. 2015. Chapter 8 - Animal models of traumatic brain injury. In: Jordan G, Andres MS, editors. Handbook of Clinical Neurology: Elsevier. p 115-128.
Johnson VE, Stewart JE, Begbie FD, Trojanowski JQ, Smith DH, Stewart W. 2013a. Inflammation and white matter degeneration persist for years after a single traumatic brain injury. Brain 136(1):28-42.
Johnson VE, Stewart W, Smith DH. 2013b. Axonal Pathology in Traumatic Brain Injury. Experimental neurology 246:35-43.
Johnson VE, Stewart W, Weber MT, Cullen DK, Siman R, Smith DH. 2016. SNTF Immunostaining Reveals Previously Undetected Axonal Pathology in Traumatic Brain Injury. Acta neuropathologica 131(1):115-135.
Kimura H, Meaney D, McGowan J, Grossman R, Lenkinski R, Ross D, McIntosh T, Gennarelli T, Smith D. 1996. Magnetization Transfer Imaging of Diffuse Axonal Injury Following Experimental Brain Injury in the Pig: Characterization by Magnetization Transfer Ratio with Histopathologic Correlation. J Comput Assist Tomogr 20(4):540-546.
Larsen MO, Rolin B. 2004. Use of the Göttingen minipig as a model of diabetes, with special focus on type 1 diabetes research. ILAR journal / National Research Council, Institute of Laboratory Animal Resources 45(3):303-313.
Lehmann H. 1998. The minipig in general toxicology. Scandinavian Journal of Laboratory Animal Science 25(SUPPL. 1):59-62.

Levin HS. 2003. Neuroplasticity following non-penetrating traumatic brain injury. Brain Injury 17(8):665-674.
Lind NM, Moustgaard A, Jelsing J, Vajta G, Cumming P, Hansen AK. 2007. The use of pigs in neuroscience: Modeling brain disorders. Neuroscience & Biobehavioral Reviews 31(5):728-751.
Marcilloux JC, Rampin O, Felix MB, Laplace JP, Albe-Fessard D. 1989. A stereotaxic apparatus for the study of the central nervous structures in the pig. Brain Research Bulletin 22(3):591-597.
Meaney DF, Smith DH, Shreiber DI, Bain AC, Miller RT, Ross DT, Gennarelli TA. 1995. Biomechanical Analysis of Experimental Diffuse Axonal Injury. Journal of Neurotrauma 12(4):689-694.
Mitra PPB, Hemant. 2007. Observed brain dynamics: Oxford University Press. 408 p.
Mitzdorf U. 1985. Current Source-Density method and application in cat cerebral cortex: investigation of evoked potentials and EEg phenomena. Physiological Reviews 65(1).
Miyazaki S, Katayama Y, Lyeth BG, Jenkins LW, DeWitt DS, Goldberg SJ, Newlon PG, Hayes RL. 1992. Enduring suppression of hippocampal long-term potentiation following traumatic brain injury in rat. Brain Research 585(1–2):335-339.
Nicholson C, Freeman JA. 1975. Theory of current source-density analysis and determination of conductivity tensor for anuran cerebellum. Journal of Neurophysiology 38(2):356.
Pampiglione G. 1971. Some aspects of development of cerebral function in mammals. Proceedings of the Royal Society of Medicine 64(4):429-435.
Park DS, Cerrone M, Morley G, Vasquez C, Fowler S, Liu N, Bernstein SA, Liu F-Y, Zhang J, Rogers CS and others. 2015. Genetically engineered SCN5A mutant pig hearts exhibit conduction defects and arrhythmias. The Journal of Clinical Investigation 125(1):403-412.
Paterno R, Metheny H, Xiong G, Elkind J, Cohen AS. 2015. Mild Traumatic Brain Injury Decreases Broadband Power in Area CA1. Journal of Neurotrauma 33(17):1645-1649.
Poceta JS, Hamlin MN, Haack DW, Bohr DF. 1981. Stereotaxic placement of cannulae in cerebral ventricles of the pig. The Anatomical Record 200(3):349-356.
Richer JP, Lacoste L, Faure JP, Hauet T, Ferrié JC, Carretier M. 1998. Sacrococcygeal and transsacral epidural anesthesia in the laboratory pig: A model for experimental surgery. Surgical and Radiologic Anatomy 20(6):431-435.
Rogers CS, Stoltz DA, Meyerholz DK, Ostedgaard LS, Rokhlina T, Taft PJ, Rogan MP, Pezzulo AA, Karp PH, Itani OA and others. 2008. Disruption of the CFTR Gene Produces a Model of Cystic Fibrosis in Newborn Pigs. Science (New York, N.Y.) 321(5897):1837-1841.
Rollin BE. 2006. The Regulation of Animal Research and the Emergence of Animal Ethics: A Conceptual History. Theoretical Medicine and Bioethics 27(4):285-304.
Rossant C, Kadir SN, Goodman DFM, Schulman J, Hunter MLD, Saleem AB, Grosmark A, Belluscio M, Denfield GH, Ecker AS and others. 2016. Spike sorting for large, dense electrode arrays. Nat Neurosci 19(4):634-641.
Saikali S, Meurice P, Sauleau P, Eliat P-A, Bellaud P, Randuineau G, Vérin M, Malbert C-H. 2010. A three-dimensional digital segmented and deformable brain atlas of the domestic pig. Journal of Neuroscience Methods 192(1):102-109.
Saito T, Bjarkam CR, Nakamura M, Nemoto T. 1998. Determination of stereotaxic coordinates for the hippocampus in the domestic pig. Journal of Neuroscience Methods 80(1):29-36.
Salinas-Zeballos M-EZ, G.A.; Gootman, P.M. 1986. A stereotaxic atlas of the developing swine (Suc scrofa) forebrain. Swine in Biomedical Research:887-906.
Schmitt S, Dichter MA. 2015. Chapter 21 - Electrophysiologic recordings in traumatic brain injury. In: Jordan G, Andres MS, editors. Handbook of Clinical Neurology: Elsevier. p 319-339.

Schomburg EW, Anastassiou CA, Buzsáki G, Koch C. 2012. The Spiking Component of Oscillatory Extracellular Potentials in the Rat Hippocampus. The Journal of Neuroscience 32(34):11798.
Sherriff FE BL, Sivaloganathan S. 1994. Early detection of axonal injury after human head trauma using immunocytochemistry for beta-amyloid precursor protein. Acta neuropathologica 87(1):55-62.
Sorensen JC, Nielsen MS, Rosendal F, Deding D, Ettrup KS, Jensen KN, Jorgensen RL, Glud AN, Meier K, Fitting LM and others. 2011. Development of neuromodulation treatments in a large animal model--do neurosurgeons dream of electric pigs? Prog Brain Res 194:97-103.
Steriade M. 1997. Synchronized activities of coupled oscillators in the cerebral cortex and thalamus at different levels of vigilance. Cerebral Cortex 7(6):583-604.
Sullivan S, Friess SH, Ralston J, Smith C, Propert KJ, Rapp PE, Margulies SS. 2013a. Behavioral Deficits and Axonal Injury Persistence after Rotational Head Injury Are Direction Dependent. Journal of Neurotrauma 30(7):538-545.
Sullivan S, Friess SH, Ralston J, Smith C, Propert KJ, Rapp PE, Margulies SS. 2013b. Improved Behavior, Motor, and Cognition Assessments in Neonatal Piglets. Journal of Neurotrauma 30(20):1770-1779.
Szteyn S, Galert D, Dynowski J, Hoczyk W. 1980. The stereotaxic configuration of hypothalamus nerve centres in the pig. Anatomischer Anzeiger 147(1):12-32.
Van Eerdenburg FJCM, Dierx JAJ. 2002. A new technique for long term, stress free, cannulation of the lateral ventricle in postpubertal, freely moving, pigs. Journal of Neuroscience Methods 121(1):13-20.
Van Gompel JJ, Bower MR, Worrell GA, Stead M, Meier TR, Goerss SJ, Chang S-Y, Kim I, Meyer FB, Marsh WR and others. 2011. Swine Model for Translational Research of Invasive Intracranial Monitoring. Epilepsia 52(6):e49-e53.
Villasana LE, Kim KN, Westbrook GL, Schnell E. 2015. Functional Integration of Adult-Born Hippocampal Neurons after Traumatic Brain Injury. eNeuro 2(5):ENEURO.0056-15.2015.
Walters EM, Wells KD, Bryda EC, Schommer S, Prather RS. 2017. Swine models, genomic tools and services to enhance our understanding of human health and diseases. Lab Anim (NY). 46(4):167-172.
Watanabe H, Andersen F, Simonsen CZ, Evans SM, Gjedde A, Cumming P. 2001. MR-based statistical atlas of the Göttingen minipig brain. NeuroImage 14(5):1089-1096.
Wiltschko AB, Gage GJ, Berke JD. 2008. Wavelet filtering before spike detection preserves waveform shape and enhances single-unit discrimination. Journal of Neuroscience Methods 173(1):34-40.
Wolf JA, Johnson, B.N., Johnson, V.E., Putt, M.E., Browne, K.D., Mietus, C.J., Brown D.P., Wofford, K.L., Smith, D.H., Grady, M.S., Cohen, A.S., Cullen, D.K. 2017. Concussion Induces Hippocampal Circuitry Disruption in Swine. Journal of Neurotrauma.
Zhang B, Chen X, Lin Y, Tan T, Yang Z, Dayao C, Liu L, Jiang R, Zhang J. 2011. Impairment of synaptic plasticity in hippocampus is exacerbated by methylprednisolone in a rat model of traumatic brain injury. Brain Research 1382:165-172.

Acknowledgements

Stereotactic Instrumentation: We would like to thank Mike Carman and Bill Pennie from the Research Instrumentation Shop at University of Pennsylvania (https://www.med.upenn.edu/ris/index.html) for co-developing the porcine stereotactic frame.

Funding: This work was made possible through financial support provided by the Department of Veterans Affairs (Rehabilitation Research & Development Career Development Award IK2-RX001479 & Merit Review Award I01-RX001097), the National Institutes of Health (NINDS R01-NS-101108-01 & T32-NS043126), CURE Foundation (Taking Flight Award), and DoD ERP CDMRP (Grant Number W81XWH-16-1-0675). None of the funding sources aided in the collection, analysis, and interpretation of data, in the writing of the report, or in the decision to submit the paper for publication.

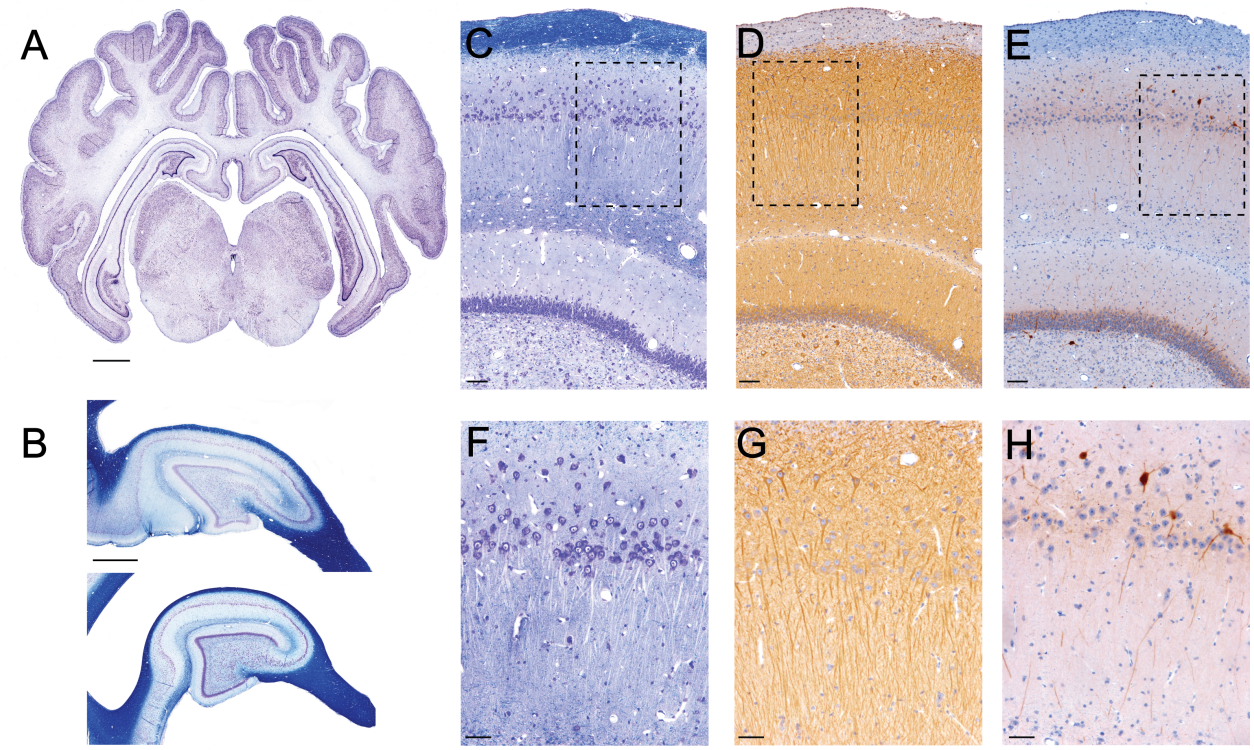

Figure 1. Morphology of Porcine Hippocampus. Sagittal and coronal sections of porcine brain were stained histologically to show organizational structure. **A)** Coronal section stained with CV showing gyrencephalic structure. Deep brain structures including hippocampus (dorsal and ventral) and thalamus are visible (scale bar = 2 mm). **B)** Coronal (top) and sagittal (bottom) sections stained with LFB/CV show white and gray matter composition in dorsal hippocampus, which can be accessed stereologically from brain surface. Both coronal and sagittal cuts through hippocampus produce arrow-like structures with anatomical layers in orientation shown (scale = 2 mm). **C-E)** Hippocampal layers including stratum oriens, pyramidal CA1 layer, striatum radiatum, lacunosum-moleculare, hippocampal fissure, striatum moleculare, and granular cell layer are clearly visible (scale bar = 100 μm). **C)** Staining with LFB shows the myelinated axons, while counterstaining with CV highlights neurons in the pyramidal and dentate cell layers. **D)** Staining with MAP2 identifies location of dendritic harbors, which are densely packed. **E)** A sub-population of interneurons is identified using parvalbumin (PV) label IHC in pyramidal and dentate granule cell layers. **F-H)** The pyramidal CA1 layer (scale bar = 50 μm). **F)** The pyramidal CA1 cell layer is widely dispersed, similar to the human CA1 layer, as shown with LFB/CV staining. **G)** Pyramidal CA1 cells send their dendrites down towards the hippocampal fissure as highlighted with MAP2 staining. **H)** PV^+ interneurons located above, inside and below pyramidal CA1 layer, send their projections into stratum radiatum.

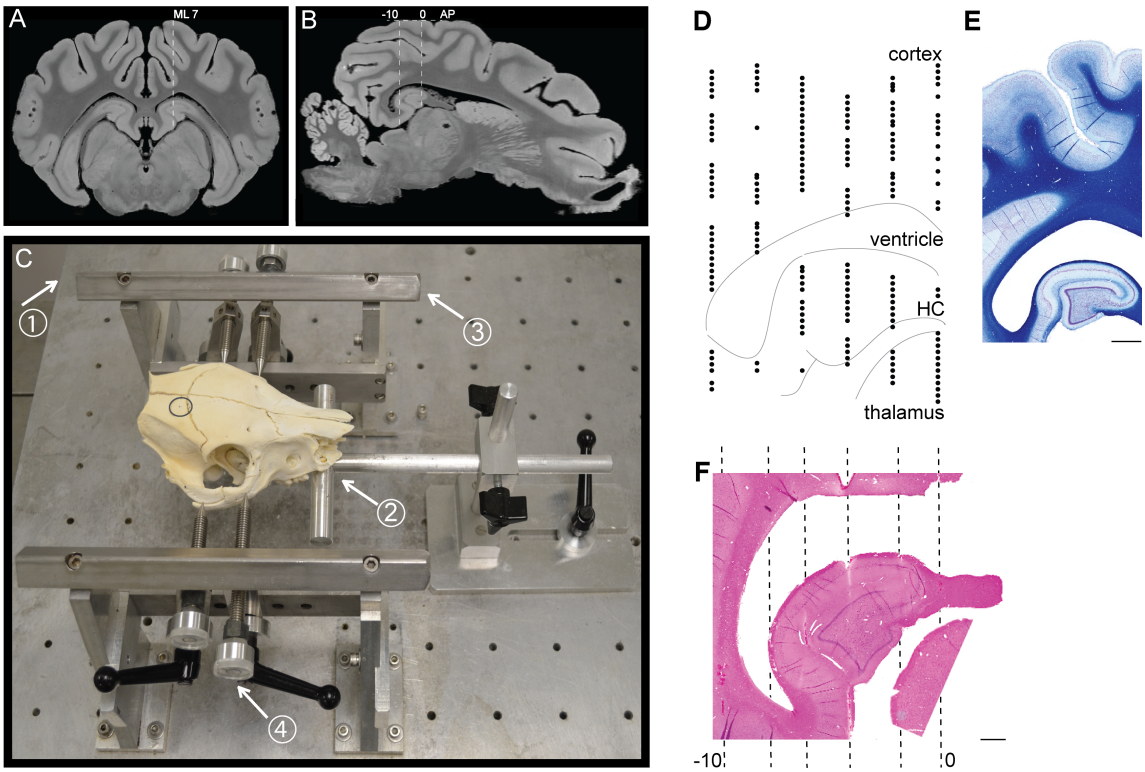

Figure 2. Novel Porcine Stereotax. The coordinates of bregma were assigned ML 0 and AP 0. Bregma is the point on the skull surface where the coronal and sagittal sutures intersect (seen in C adjacent to circle). The approximate projection of bregma into the brain in the sagittal plane was estimated using a stereotaxic atlas of the pig brain. **A)**. A coronal section through bregma taken from the MRI atlas shows the orientation of deep structures such as dorsal and ventral hippocampi (Saikali et al., 2010). We selected ML 7 as an access plane to the widest part of dorsal hippocampus. **B)** A sagittal section through ML 7 taken from the MRI atlas shows position and approximate size of the dorsal hippocampus. The image was rotated so that cortex above hippocampus is in the horizontal plane (horizontal dashed line). An approximate size of the hippocampus is shown between vertical dashed lines from right (AP 0) to left (AP -10). **C)** Photograph of a pig skull *in situ* in the stereotaxic instrument. The main parts of the stereotaxis are frame base (1), bite bar (2), anterior-posterior (AP) bars (3), and pins (4). The animal's head is first guided between AP bars and onto an adjustable bite bar, then a set of four pins is inserted into the zygomatic bones. Location and size of the craniectomy are shown (black circle). **D)** ML coordinates obtained with this stereotax are fairly accurate, but AP coordinates are not, therefore functional mapping is needed for each experiment. A representative digitized tungsten map is shown in the AP plane at ML 7. The lines outline deep brain structures including cortex, ventricle, hippocampus, and thalamus, which can be compared to the representative sagittal section **(E)**, stained with LFB/CV (scale bar = 2 mm). **F)** A representative sagittal section, cut from the same animal and stained with H&E (scale bar = 1 mm), contains Hamilton syringe tracks done in the AP plane by going in 2mm steps from AP 0 to AP -10 (dashed lines).

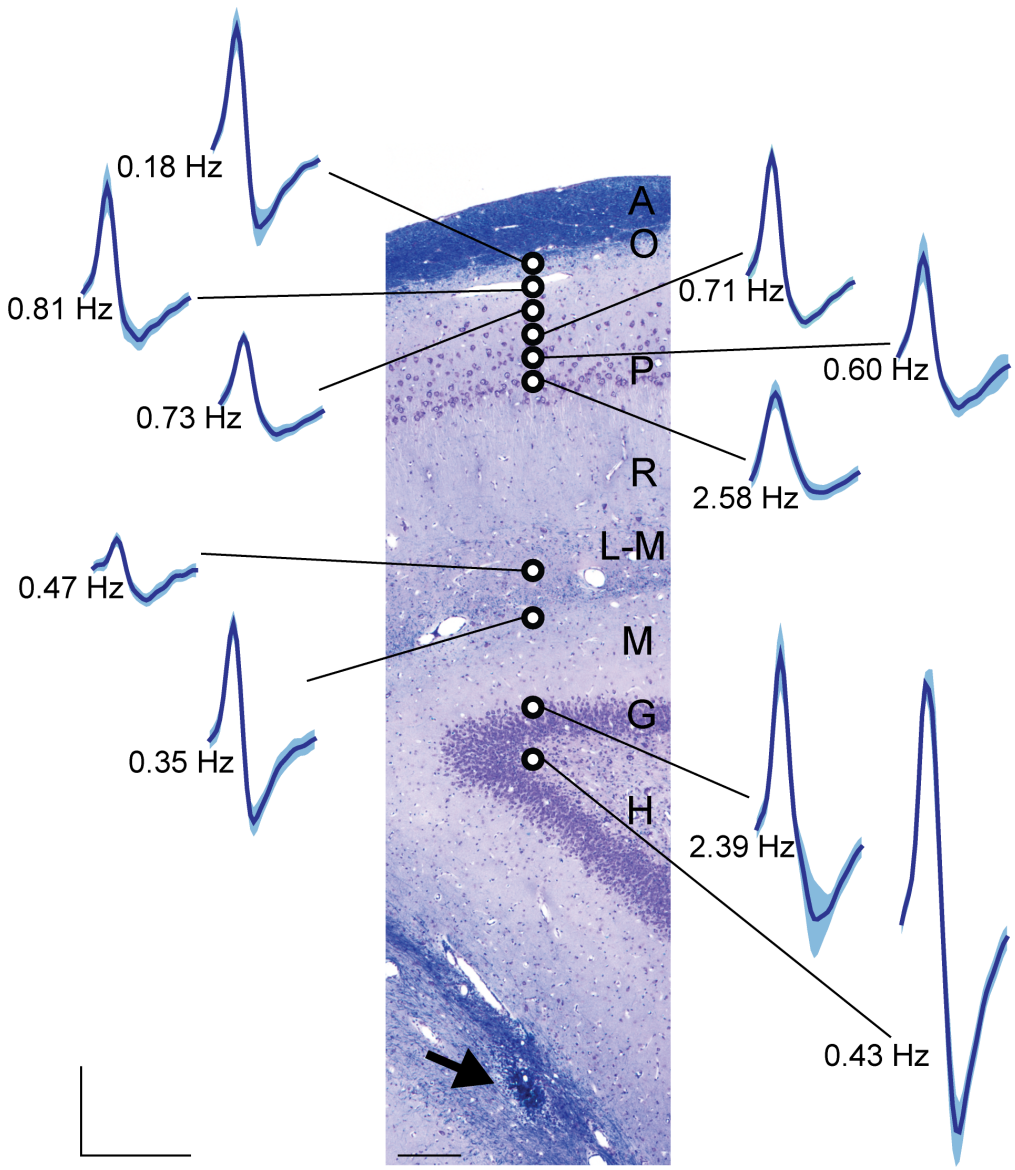

Figure 3. Single Unit Recordings in Porcine Hippocampus Corroborate Laminar Structure. A coronal section of the dorsal hippocampus stained with LFB/CV is shown from the same animal from which high impedance recordings were made during the mapping procedure (scale bar = 100 μm). Histologically identified layers are labeled. Tip of depth silicon probe placed at the end of the experiment (DV = 25) is indicated by the black arrow. A thin tungsten electrode was slowly advanced along the indicated track. Three minute recordings were made at regular intervals spaced 100-200 μm apart. Raw neural signals were processed offline and putative single units were isolated. Depths at which single units were successfully isolated are indicated by black and white circles. Representative cells from each hippocampal layer are shown as an averaged wave form accompanied by firing rate (scale bar: X axis – 1 msec; Y axis – 100 μV). A=stratum alveus, O=stratum oriens, P=stratum pyramidale, R=stratum radiatum, L-M=stratum lacunosum-moleculare, M=stratum moleculare, G=stratum granulosum, H=hilus.

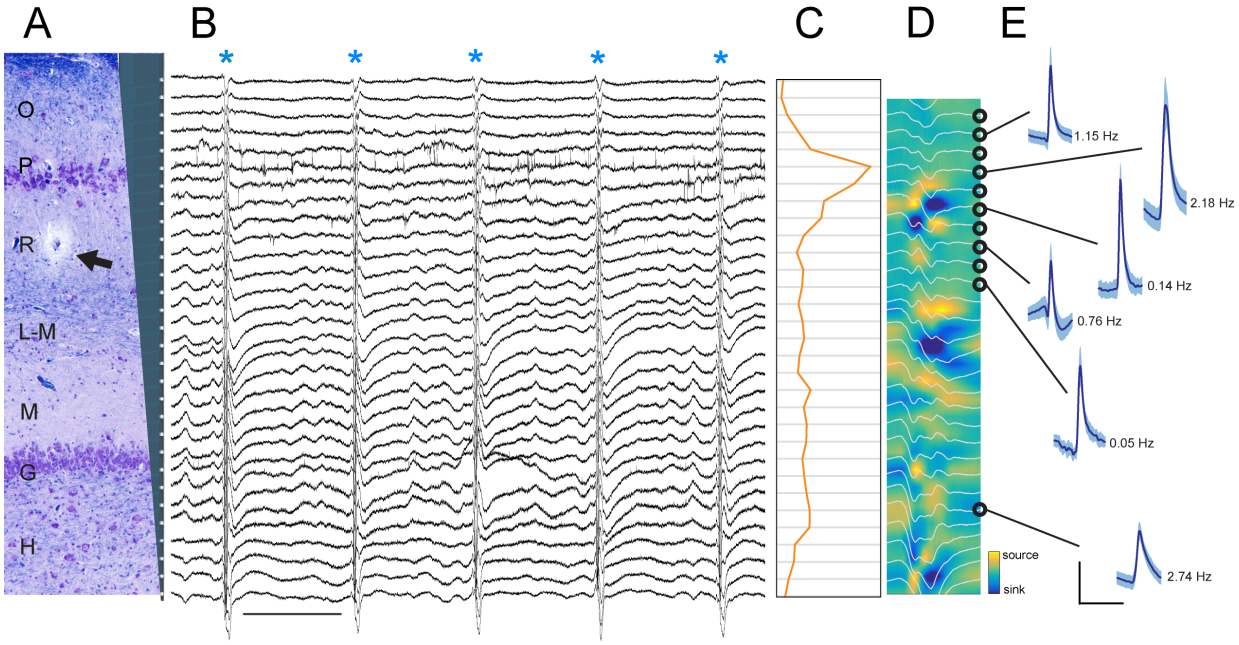

Figure 4. Laminar Structure of Extracellular Recordings Reveals Electrode Position. **A**) Coronal section of the dorsal hippocampus stained with LFB/CV is approximately aligned to extracellular recordings from the same animal (B-D) along the vertical axis (scale bar = 100 μm). Distinct hippocampal layers can be seen and are labeled. A 32-channel silicon probe was inserted into the dorsal hippocampus based on the initial functional mapping. Arrow points to artifact from electrode track. Electrical activity (B-E) is shown at final position of the electrode. (B-D) are aligned to the 31 recording channels of the silicon electrode along the vertical axis (200 μm spacing), indicated by gray cartoon of electrode along right side of (A). Alignment was based on recovered artifact of electrode tip (not shown), stereotactic coordinates used during insertion and electrophysiological features (B-E). Vertical alignment is only approximate as the plane of insertion was oblique to the histological coronal plane and the relative thicknesses of hippocampal layers' change along the AP axis. **B**) Six second tracing of wide-band LFP across all channels. Note regular bursts of synchronized input that occur approximately every 1 second (blue asterisks), likely representing cortical bursts (scale bar = 1 sec). Multi-unit spiking activity can be seen in two distinct bands: dorsal band indicating stratum pyramidale and ventral, smaller band indicating stratum granulosum. **C**) Orange line represents integrated spectral power in the 100-200 Hz band across all channels with its peak within stratum pyramidale. **D**) CSD map with superimposed LFP of 200 msec average of all detected cortical bursts (examples indicated by blue asterisks in (B)). Sinks in the proximal dendritic tree of the pyramidal cells (stratum radiatum) and in their distal dendritic tree (stratum lacunosum-moleculare) are visible, as well as a large sink within the hilus. Sources corresponding to the pyramidal and granular cell layers are also visible, as well as at the border of stratum radiatum and lacunosum-moleculare. **E**) Open circles indicate channels on which single spiking units were isolated revealing a large cluster in the region of stratum pyramidale and a single channel in the region of stratum granulosum (scale bar: X axis – 2 msec, Y axis - 100 μV). Examples of isolated spike waveforms displayed as mean ± standard deviation (blue band) are shown. O=stratum oriens, P=stratum pyramidale, R=stratum radiatum, L-M=stratum lacunosum-moleculare, M=stratum moleculare, G=stratum granulosum, H=hilus.